Optimization of 1.3 μm GaAs-based oxide-confined (GaIn)(NAs) vertical-cavity surface-emitting lasers for low-threshold room-temperature operation

Optimization of 1.3 μm GaAs-based oxide-confined (GaIn)(NAs) vertical-cavity surface-emitting lasers for low-threshold room-temperature operation

Robert P Sarzała[1] **and Włodzimierz Nakwaski**[1,2]

[1] Institute of Physics, Technical University of Łódź, ulica Wólczańska 219, 93-005 Łódź, Poland
[2] Center for High Technology Materials, University of New Mexico, Albuquerque, NM 87106, USA

E-mail: rpsarzal@p.lodz.pl

Abstract
In this paper, use of a comprehensive self-consistent optical–electrical–thermal–gain threshold model of oxide-confined GaAs-based (GaIn)(NAs)/GaAs quantum-well vertical-cavity surface-emitting diode lasers (VCSELs) is demonstrated. The model was developed to facilitate better understanding of the physics of operation of the above devices including the full complexity of the many interactions, in the volumes of the devices, between individual physical phenomena. Besides this, the model was applied in designing and optimizing such VCSELs for long-wavelength 1.3 μm second-generation optical fibre communication system use and for examining their anticipated continuous-wave (CW) room-temperature (RT) low-threshold performance. The influences of many construction parameters on device CW RT lasing thresholds and mode selectivity were investigated. Some essential design guidelines were proposed to support efforts of technological centres to produce low-threshold single-mode RT CW devices. In particular, the 1.5λ-cavity VCSELs have been found to exhibit lower RT CW lasing thresholds, whereas the 3λ-cavity ones offer better thermal properties: higher values of the parameter T_0 and single-fundamental-mode operation possible at higher temperatures. As expected, the desired stable RT CW single-fundamental-mode operation is possible in smaller VCSELs (with active-region diameters not exceeding 6 μm in the case of the 1.5λ-cavity VCSELs). A deliberate detuning of the lasing mode from the RT active-region optical peak gain towards higher wavelengths ensures better device operation at higher temperatures.

1. Introduction

In modern short- and medium-distance optical fibre links ($<$50 km), the cost of the transmitter devices represents quite a significant fraction of the system cost. Therefore relatively costly

InP-based diode lasers seem to be too expensive to underpin a big market in long-wavelength optical fibre metro-area (MAN) and local-area (LAN) communications (Pessa *et al* 2003, Anscombe 2003). Moreover, their high-temperature performance is still very poor and the efficiencies of the radial confinements of current spread and optical fields are not satisfactory. Besides this, the vertical-cavity surface-emitting laser (VCSEL) structure is believed to be the laser configuration best suited for optical transmitters. This follows from its inherently single-longitudinal-mode operation, ease of fibre coupling, facility of modulation and the straightforward fabrication of two-dimensional arrays. Unfortunately, InP-based VCSELs are technologically even more complex than edge-emitting lasers.

On the other hand, the well-established low-cost fabrication of GaAs-based VCSEL devices ensures their extremely high reliability, relatively simple manufacturing of highly reflective distributed-Bragg-reflector (DBR) mirrors as well as easy creation of efficient radial confinements, both electrical and optical, with the aid of oxide apertures produced by selective radial oxidation of AlAs-rich layers. Therefore, the 850 nm GaAs-based VCSELs, emitting in the so-called 'first window' of silica fibres, are currently used in short- and medium-distance 100 Mb s^{-1} optical networks. For slightly longer carrier wavelengths, up to 980 nm, VCSELs with GaInAs quantum-well (QW) active layers and GaAs-based DBRs may be manufactured. However, due to the ongoing problems associated with the growth of high-optical-quality GaInAs material, their efficiencies are often not as high as those predicted by theoretical models.

The recently observed enormous growth of demand for higher-rate communication systems is associated with the Internet and data-transmission needs: the high-rate (1 Gb s^{-1} or even 10 Gb s^{-1}) networks predicted for the near future. The 'second-window' 1.3 μm optical links with much lower optical losses and minimal dispersion offer real hope of a prospective solution. However, it is essential to take advantage of the outstanding arsenide technology; therefore quaternary (GaIn)(NAs)/GaAs QWs, first proposed by Kondow *et al* (1996), which enable laser emission in the 1.3 μm band and ensure excellent high-temperature performance because of the large conduction-band offset, are becoming seen as a very promising new material system.

Thus the oxide-confined GaAs-based VCSELs with (GaIn)(NAs)/GaAs quantum wells seem to be the best laser candidates for future mass 1.3 μm metro-area and local-area optical fibre communication network use (Harris 2001, Steinle *et al* 2001b, Riechert *et al* 2002, Pessa *et al* 2003). The first 1.3 μm (GaIn)(NAs)/GaAs VCSELs have already been manufactured (e.g. Coldren *et al* 2000, Larson *et al* 2000, Steinle *et al* 2001a, 2001b, Ramakrishnan *et al* 2003). But this relatively immature device still requires some physical modelling to examine its special features as well as to discover its strong and weak points and finally to enable design of the best high-performance, low-threshold 1.3 μm diode VCSELs. Accordingly, in the present paper, the threshold operation of oxide-confined GaAs-based (GaIn)(NAs)/GaAs VCSELs is accurately simulated and carefully analysed to enable their optimization for low-threshold room-temperature (RT) continuous-wave (CW) operation and to support the proposal of some technological guidelines for their successful design.

2. The model

Our model comprises five interrelated parts, describing (dealt with in successive subsections) the band structure of the (GaIn)(NAs)/GaAs quantum well as well as electrical, optical, thermal and gain processes crucial for the laser operation. Our description of the model is followed by an explanation of all essential interactions between various physical phenomena. General rules for the advanced modelling of VCSEL operation were formulated by Osiński and Nakwaski (2003).

Table 1. The α and β parameters used in equation (2).

Material	α (10^{-4} eV K^{-1})	β (K)	Reference
GaAs	5.405	204	Thurmond (1975)
GaInAs	5.408	204	Skierbiszewski (2002)
GaInNAs	5.5	384	Shirakata *et al* (2001)

2.1. The (GaIn)(NAs)/GaAs quantum well

Determination of a QW band structure and its energy levels needs knowledge of values of the band-gaps, the effective masses and the band offset. The RT value of the band-gap of the $\text{Ga}_{1-x}\text{In}_x\text{N}_y\text{As}_{1-y}$ material is taken from the band anti-crossing model in the following form (Shan *et al* 2001):

$$E_{\text{GaInNAs}}(x, y) = \tfrac{1}{2}\Big[E_{\text{GaInAs}}(x) + E_{\text{N}}(x) - \sqrt{[E_{\text{GaInAs}}(x) - E_{\text{N}}(x)]^2 + 4yC_{\text{MN}}^2(x)}\Big] \qquad (1)$$

with $E_{\text{N}}(x) = 1.65 - 0.4x(1 - x)$ and $C_{\text{MN}}(x) = 2.7 - 2.68x$ (Hetterich *et al* 2003). The band-gap for GaAs at 0 K is found from (Blakemore 1983): $E_{\text{GaAs}}(0\text{ K}) = 1.519$ eV, and the analogous band-gap for the $\text{Ga}_{1-x}\text{In}_x\text{As}$ material from (Skierbiszewski 2002): $E_{\text{GaInAs}}(x, 0\text{ K}) = (1.512 - 1.337x + 0.27x^2)$ eV. For other temperatures, the band-gaps are determined from the Varshni relation:

$$E(T) = E(0\text{ K}) - \frac{\alpha T^2}{\beta + T} \qquad (2)$$

where the α and β values are listed in table 1.

On the basis of data reported in Hetterich *et al* (2000), Tansu and Mawst (2003), Tomic and O'Reilly (2002), the band offset ratio for the (GaIn)(NAs) material is assumed to be 0.80/0.20 and the matrix element is assumed to be 9.33 m_0 eV. The electron effective mass: $m_{\text{e}}^* = 0.137\ m_0$ is taken from Carrére *et al* (2003), and those for the heavy hole: $m_{\text{hh}}^* = 0.518\ m_0$ and the light hole: $m_{\text{lh}}^* = 0.156\ m_0$ from Seo and Donegan (2003) and Lencefield *et al* (1995), respectively.
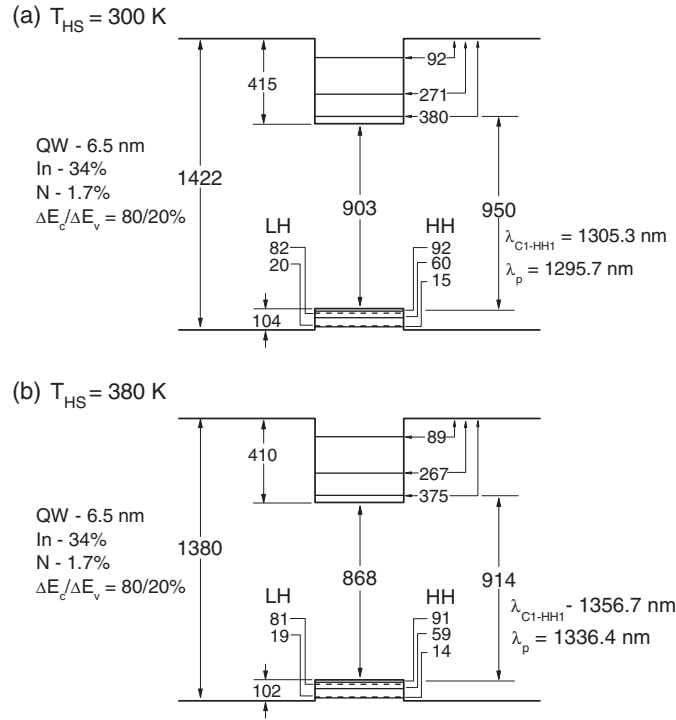
The band structures of the $\text{Ga}_{0.66}\text{In}_{0.34}\text{N}_{0.017}\text{As}_{0.983}$/GaAs 6.5 nm QW at RT (300 K) and at 380 K are presented in figures 1(a) and (b), respectively. As one can see for both temperatures, three energy levels are contained within the QW for electrons and heavy holes and only two for light holes. As expected, with increase in temperature, all band-gaps and energy levels are shifted towards lower energies. The λ_p wavelengths, corresponding to the maxima of the gain spectra, are somewhat lower than the $\lambda_{\text{C1-HH1}}$ ones, determined for the transitions from the first electron level to the first heavy-hole level.

2.2. The electrical model

The finite-element (FE) electrical model of the laser takes into account in a natural way the interplay of drift and diffusion currents of both electrons and holes. The current spread is determined from the three-dimensional (3D) potential distributions $V(r, z, \varphi)$ found by solving the Laplace equation:

$$\text{div}[\sigma(r, z, \varphi)\text{grad}(V(r, z, \varphi))] = 0 \qquad (3)$$

where σ stands for the 3D profile of the electrical conductivity, and r, z and φ compose the cylindrical coordinate system with the $0z$ axis directed along the device axis. From now on, we use the following notation: $\vec{r} = (r, z, \varphi)$. For all layers of the laser structure (with the

Figure 1. Band structures of the $Ga_{0.66}In_{0.34}N_{0.017}As_{0.983}$/GaAs 6.5 nm quantum well at (a) 300 K and (b) 380 K. All dimensions are given in meV. The wavelength values λ_p, corresponding to the maxima of the gain spectra, and λ_{C1-HH1}, determined for the transitions from the first electron level to the first heavy-hole level, are shown.

exception of the active region), the above conductivity σ depends on the material composition and its doping, as well as on the local temperature and local carrier concentration (Nakwaski and Osiński 1993). Generation and recombination phenomena within the active region are usually sources of a non-zero right-hand side of equation (3) (known as the Poisson equation in this case). Their relative influence is difficult to analyse theoretically; therefore they have been taken into account symbolically in the model with the aid of the effective conductivity σ_{pn} of the active-region material. Its value is found using the differential Ohm law and the classical diode equation:

$$\sigma_{pn}(r) = \frac{\beta_{pn} j_{pn}(r) d_{A,E}}{\ln\left[\frac{j_{pn}(r)}{j_s} + 1\right]} \tag{4}$$

where j_{pn} is the p–n junction current density and $d_{A,E} = 25$ nm (GaAs)$+2 \times 6.5$ nm (GaInNAs) $= 38$ nm stands for the cumulative active-region thickness including not only QW layers but also the barrier layers between them, $\beta_{pn} = 19$ V^{-1} is the diode parameter and $j_s = 1.1$ A m^{-2} stands for the saturation current density.

To obtain the 3D potential profile for the whole laser structure, it should be matched (using the self-consistent approach) with the aid of boundary conditions at all boundaries between the layers. Then the 3D current density distribution $j(\vec{r})$ throughout the whole device volume may be found from the differential Ohm law:

$$j(\vec{r}) = -\sigma(\vec{r})\text{grad}[V(\vec{r})]. \tag{5}$$

Afterwards, the carrier density profile $n_A(r)$ within the active layer may be determined from the below-threshold diffusion equation:

$$D_A \left[\frac{\partial^2 n_A(r)}{\partial r^2} + \frac{1}{r} \frac{\partial n_A(r)}{\partial r} \right] - An_A(r) - Bn_A^2(r) - Cn_A^3(r) + \frac{j_{pn}(r)}{ed_A} = 0 \tag{6}$$

where $D_A = 10$ cm^2 s^{-1} (Sarzała and Nakwaski 1997) is the ambipolar diffusion coefficient and the recombination coefficients for temperatures within the 300–350 K range are extracted from data reported by Fehse *et al* (2002) in the following forms:

$$A = (138.06 - 0.109T)10^7 \text{ s}^{-1} \tag{7a}$$
$$B = (25.35 - 0.0562T)10^{-11} \text{ cm}^3 \text{ s}^{-1} \tag{7b}$$
$$C = (-6.22 + 0.0344T)10^{-29} \text{ cm}^6 \text{ s}^{-1}. \tag{7c}$$

2.3. The optical model

Currently, the most advanced scalar optical VCSEL model, known as the effective frequency model (EFM), is that proposed by Wenzel and Wünsche (1997). In the model, the structure eigenmodes are assumed to be of the following form:

$$E(\vec{r}, t) = E(\vec{r}) \exp(i\omega t) \tag{8}$$

with a complex mode frequency

$$\omega = \omega' + i\omega'' \tag{9}$$

accounting for possible loss and gain effects within the optical cavity.

Assuming circular symmetry of a VCSEL geometry, the optical field may be separated into two one-dimensional approximating functions:

$$E(\vec{r}) = f(r, z)\Phi_L(r) \exp(iL\varphi) \qquad L = 0, 1, 2, \dots \tag{10}$$

where L is the azimuthal mode number. The axial part of the solution is assumed to be normalized:

$$\int_0^{L_L(r)} f^2(r, z) \, dz = 1 \tag{11}$$

where $L_L(r)$ corresponds to the resonator length at the radius r. Finally, the complex optical fields in VCSEL resonators are taken, for simplicity, to be governed by two mutually interrelated nearly one-dimensional wave equations along the axial and radial directions:

$$\left[\frac{d^2}{dz^2} + k_0^2 n_R^2(r, z) \right] f(r, z) = v_{eff}(r) k_0^2 n_R(r, z) n_g(r, z) f(r, z) \tag{12}$$

$$\left[\frac{d^2}{dr^2} + \frac{1}{r} \frac{d}{dr} - \frac{L^2}{r^2} + v_{eff}(r) k_0^2 \langle n_R n_g \rangle_r \right] \Phi_L(r) = v k_0^2 \langle n_R n_g \rangle_r \Phi_L(r) \qquad L = 0, 1, 2, \dots \tag{13}$$

where v_{eff} is the effective frequency, $k_0 = \omega_0/c$ is the vacuum wavenumber and ω_0 is the real-valued nominal angular frequency corresponding to the designed periodicity of the DBR mirrors. $n_R(\vec{r}, \omega_0)$ and $n_g(\vec{r}, \omega_0)$ are the complex refractive phase and group indices, respectively, evaluated at the nominal angular frequency ω_0. The dimensionless complex parameter v plays the role of an eigenvalue and is defined as

$$v \equiv 2\frac{\omega_0 - \omega}{\omega_0} = 2\frac{\lambda - \lambda_0}{\lambda} - i\frac{2\omega''}{\omega_0}. \tag{14}$$

Its real part describes the relative wavelength shift from the nominal wavelength λ_0, whereas its imaginary part is the relative decay constant of the corresponding mode. $\langle n_R n_g \rangle_r$ may be written in the following form:

$$\langle n_R n_g \rangle_r = \int_0^{L_L(r)} n_R(r,z) n_g(r,z) f^2(r,z) \, dz. \tag{15}$$

Assuming outgoing plane waves at the bottom ($z = 0$) and the top ($z = L_L$) surfaces of the laser cavity, the following axial boundary conditions may be formulated:

$$\frac{df}{dz} \pm i k_z f = 0 \qquad z = \left\{ \begin{array}{c} L_L(r) + \varepsilon \\ 0 - \varepsilon \end{array} \right\} \tag{16}$$

where ε is a small positive number and $k_z = k_0(n_R^2 - \nu_{eff} n_R n_g)$. So the structure is divided into a number of cylindrically symmetric ring sectors. Constant and uniform distributions of refractive indices and of loss and gain coefficients within every individual layer and every individual sector are assumed—but they may be different in different layers and in different sectors.

Analogously, the $\Phi_L(r)$, $L = 0, 1, 2, \ldots$, are assumed to satisfy the following boundary conditions, ensuring a cylindrical outgoing wave at sufficiently large radial distance r_∞:

$$\frac{d\Phi_L(r)}{dr} + \frac{\Phi_L(r)}{2r} + i k_r \Phi_L(r) = 0 \qquad r = r_\infty \tag{17}$$

where $k_r = k_0[(\nu_{eff} - \nu)\langle n_R n_g \rangle_r]^{1/2}$. The radial field is determined for a structure averaged in the z direction, as if the waveguide were uniform, although slow radial changes of losses (or gains) and refractive indices are also included.

The algorithm needs to be a self-consistent procedure because the effective frequency is present in both nearly one-dimensional wave equations (12) and (13).

2.4. The thermal model

The FE thermal model of the laser solves the heat-conduction equation for the whole structure using the same mesh as was generated for the FE electrical calculations:

$$\text{div}[\lambda_T(\vec{r}) \text{grad}(T(\vec{r}))] = -g_T(\vec{r}). \tag{18}$$

In the above equation, λ_T stands for the thermal conductivity coefficient (in W m^{-1} K^{-1}) and g_T is the volume density of heat sources (in W m^{-3}). The thermal conductivity of the oxidized Al_xO_y layer is assumed to be equal to that of the sapphire (Al_2O_3) (Babić *et al* 1999) and those of the semiconductor layers are taken from Nakwaski (1988). Non-radiative recombination and reabsorption of spontaneous radiation is found to constitute the main heat source located within the active region of the laser. Additionally, the volume Joule heating in all structure layers and the barrier Joule heating in the contacts are taken into account. The 3D heat-flux spread in a copper heat sink is determined assuming its external walls to be kept at the ambient RT. Side and top laser-crystal walls are assumed to be thermally isolated because both the thermal radiation and the thermal convection of air particles are negligible compared with the intense heat-flux conduction through the bottom device base into its heat sink.

2.5. The gain model

In the calculation of the optical gain, the classical Fermi golden rule and the parabolic band-gap approximation are assumed (Chuang 1995). The optical gain spectra g may then be determined from the following relation:

$$g(\hbar\omega) = \sum_m \int_{-\infty}^{\infty} g_m(\varepsilon) \Lambda(\hbar\omega - \varepsilon) \, d\varepsilon \tag{19}$$
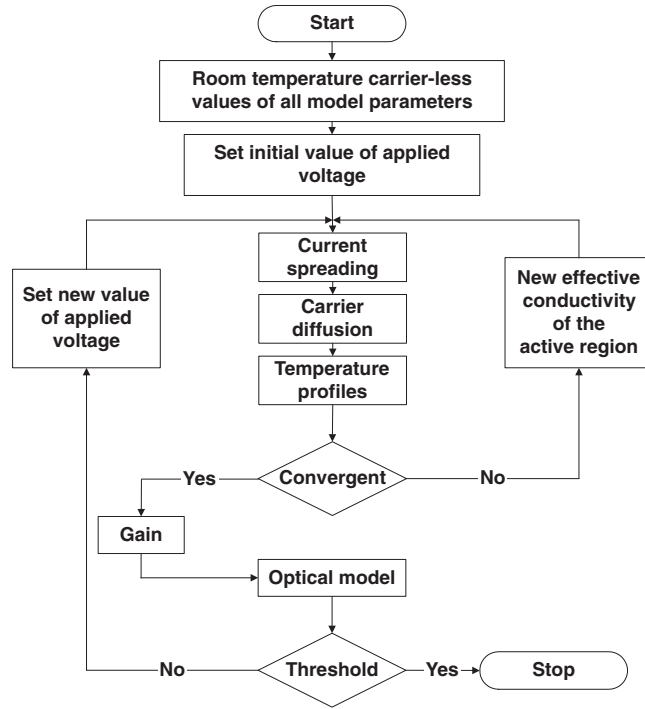
Figure 2. A flowchart of the self-consistent calculation algorithm used in our modelling.

where the summation should be carried out over all available numbers m of level pairs and

$$g_m(\hbar\omega) = \frac{e^2\pi\hbar}{n_R c m_0^2 \varepsilon_0} \frac{M^2 \rho_r^{2D}(\hbar\omega)}{\hbar\omega} \{f_c[E_e(m,\hbar\omega)] - f_v[E_h(m,\hbar\omega)]\} \qquad (20)$$

where n_R stands for the index of refraction, c is the speed of light in vacuum, m_0 is the rest electron mass, ε_0 is the vacuum dielectric constant, M is the momentum matrix element, ρ_r^{2D} stands for the two-dimensional reduced density of states, f_c and f_v are the Fermi–Dirac functions determined for electrons in the conduction band and for holes in the valence band, respectively, E_e and E_h are the energies of the recombining electron and hole, respectively, and Λ is the broadening function (Eliseev 1997), usually of Lorentzian type.

2.6. Interactions between individual physical phenomena

Our model considers all important interactions between individual physical phenomena, including:

 (1) thermal focusing, i.e. the temperature dependence of refractive indices;
 (2) temperature dependence of the thermal conductivities;
 (3) temperature, dopant and carrier-concentration dependences of the electrical conductivities;
 (4) temperature and carrier-concentration dependences of the active-region energy gap.

Accordingly, 3D profiles of all model parameters are determined not only on the basis of various chemical compositions of structure layers but also taking into account 3D profiles of the temperature, current density, radiation intensity and carrier concentration within the whole device volume, all of them with the aid of a self-consistent calculation algorithm. The self-consistent calculation algorithm is shown in figure 2.
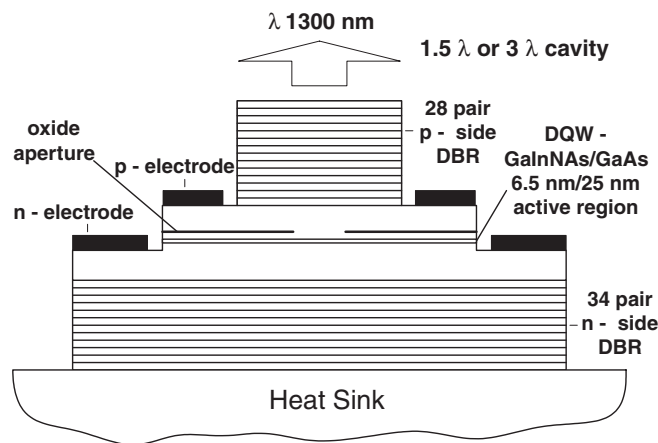
Figure 3. The typical structure of the 1.3 μm GaAs-based oxide-confined (OC) (GaIn)(NAs)/GaAs double quantum-well (DQW) vertical-cavity surface-emitting laser (VCSEL).

Table 2. Compositions and thicknesses of structure layers of the 1.5λ-cavity VCSEL. Some values of model parameters are also given.

Layer	Thickness (nm)	Refractive index n_R	dn_R/dT $(10^{-4}\ K^{-1})$	Group refractive index n_G	Absorption coefficient α (cm^{-1})	$d\alpha/dT$ $(1/10^3\ cm\ K)$
GaAs upper DBR	28×95.6	3.4	2.0	3.654	5	1.28
Al$_{0.8}$Ga$_{0.2}$As upper DBR	28×108	3.01	1.47	3.198	5	1.28
p-GaAs	184.7	3.4	2.0	3.654	50	1.28
Al$_x$O$_y$	15	1.61	0	1.681	50	0
p-GaAs	165.2	3.4	2.0	3.654	10	1.28
Ga$_{0.66}$In$_{0.34}$N$_{0.017}$As$_{0.983}$ quantum well	2×6.5	3.8	3.0	4.62	0	0
GaAs barrier	25	3.4	2.0	3.654	0	0
n-GaAs	171.6	3.4	2.0	3.654	5	1.28
GaAs bottom DBR	34×95.6	3.4	2.0	3.654	1	1.28
AlAs bottom DBR	34×111.5	2.915	1.34	3.056	1	1.28

3. The structure

Let us consider a typical structure of a 1.3 μm oxide-confined (OC) GaAs-based (GaIn)(NAs)/GaAs QW VCSEL, as shown in figure 3. The thicknesses (for the 1.5λ-cavity VCSELs) and compositions of all its structure layers are given in table 2, where additionally numerical values of some model parameters are given. They are taken from the following references: Deria and Emanuel (1995) and Sato *et al* (1997)—refractive indices of semiconductor layers; Sfigakis *et al* (2000) and http://www.ioffe.rssi.ru—refractive indices of Al$_x$O$_y$; Grimmeiss and Monemar (1971)—temperature variations of refractive indices; Tanguy (1996), Grimmeiss and Monemar (1971) and Kitatani *et al* (1998)—group refractive indices;
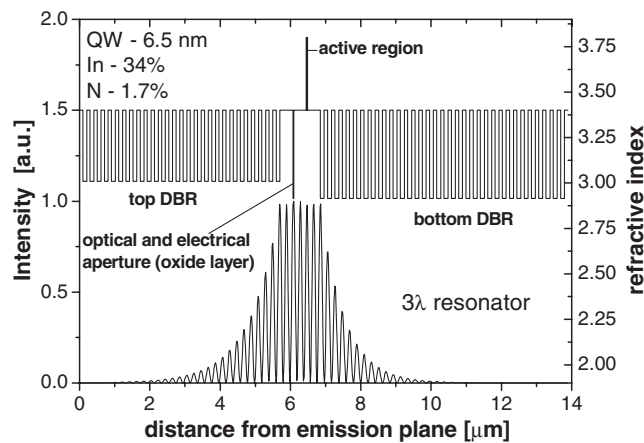
Figure 4. The standing wave of the LP$_{01}$ mode in the 3λ VCSEL resonator. The profile of an index of refraction is also shown.

Adachi (1994)—absorption coefficients; and Spitzer and Whelan (1959)—their temperature changes. The temperature variations of the refractive indices are determined for (GaIn)(NAs) using the method reported by Tanguy (1996).

The laser-active region is similar (but not identical) to the one reported by Infineon Technologies AG, i.e. by Steinle *et al* (2001a, 2001b), Riechert *et al* (2002) and Ramakrishnan *et al* (2003). It consists of two 6.5 nm (GaIn)(NAs) QWs (double QW (DQW) structure), each containing about 35% indium and 1.5–1.8% nitrogen, separated by a 25 nm GaAs barrier, both intentionally undoped (residual 10^{16} cm^{-3} doping is assumed). The active region is sandwiched by p-type and n-type GaAs spacers. Whereas the upper part (over the oxide aperture) of the p-type spacer is doped to 2×10^{18} cm^{-3}, the lower one (between the oxide and the active region) is doped only to 10^{17} cm^{-3}. Analogously, the upper part (between the active region and the base of the mesa structure) of the n-type spacer is doped to only 10^{16} cm^{-3}, whereas the bottom one is doped to 10^{18} cm^{-3}. Relatively high doping of the upper part of the p-type spacer and the bottom part of the n-type one is used to reduce their electrical resistivities because they are also working as radial-current-spreading layers for a current flow from annular contacts towards the central active region. 28 periods of quarter-wave GaAs/Al$_{0.8}$Ga$_{0.2}$As layers (of total reflectivity 99.9350%) and an analogous 34 periods of GaAs/AlAs layers (99.9943%) are assumed as the top and bottom, respectively, DBR resonator mirrors. Their diameters are 50 and 100 μm, respectively. Two (n side and p side) annular contacts are deposited on both GaAs spacer layers (see figure 3). The internal contact diameters are postulated to be 54 μm (p side) and 74 μm (n side), respectively, whereas the external ones are postulated to be 70 and 100 μm. Typical values of their contact resistances are 10^{-5} Ω cm^2 (n side) and 10^{-4} Ω cm^2 (p side) (the reported values, see e.g. Aboelfotoh *et al* (1999), Ueng *et al* (2001), are even (much) lower).

A radial selective oxidation (transforming AlAs into Al$_x$O$_y$ native oxides) is proposed to create within the p-type GaAs spacer an oxide aperture working as both the electrical (to funnel current spreading from the annular contact towards the central active region) and the optical (to confine the optical field in a radial direction) apertures, of assumed diameter $\phi = 2r_A$. The nominal thickness of the oxide apertures is assumed to be 15 nm.

Two resonator configurations, namely the 1.5λ cavity and the 3λ cavity, are considered. Both the active region and the oxide aperture are assumed to be located exactly in the anti-node position of the optical standing wave (figure 4).
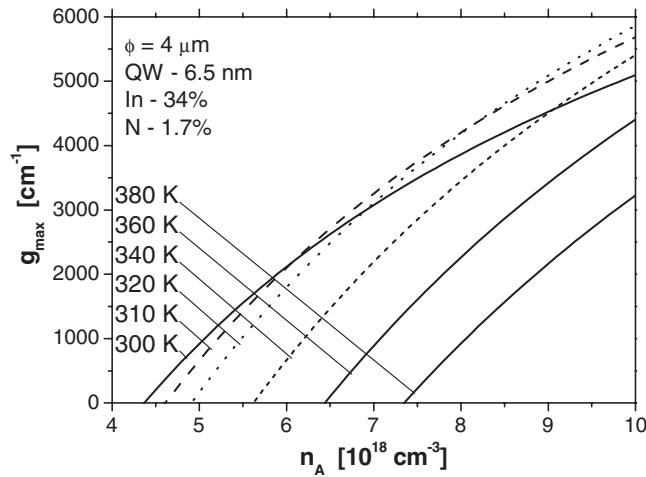
Figure 5. The maximal optical gain, g_{max}, versus the active-region carrier concentration, n_A, determined for the 6.5 nm $Ga_{0.66}In_{0.34}N_{0.017}As_{0.983}$/GaAs QW at various temperatures.

4. Results

The main results of our simulation are presented in successive figures. All curves concern the CW operation at given temperatures. If not indicated otherwise, ambient RT (300 K), the 6.5 nm $Ga_{0.66}In_{0.34}N_{0.017}As_{0.983}$/GaAs DQW active region and its diameter $\phi = 4~\mu$m are assumed.

4.1. Optical gain

Figure 5 presents the maximal optical gain versus the active-region carrier concentration determined for the 6.5 nm $Ga_{0.66}In_{0.34}N_{0.017}As_{0.983}$/GaAs QW at given temperatures. A continuous increase in the transparency concentration n_{tr}, for which $g(n_{tr}) = 0$, is observed for increasing temperatures. Saturation effects are noticed, most distinctly for lower temperatures. Both of the above effects strongly influence the high-temperature and high-power device behaviour.

4.2. The 1.5λ-cavity VCSELs

First let us consider the typical 1.5λ-cavity VCSELs. The active-region radial profiles of a threshold optical gain g_{th} at various temperatures are plotted in figure 6. Maximal values of the threshold active-region carrier concentrations are indicated. With increase in temperature, gain profiles become very non-uniform surprisingly quickly. While at RT (300 K) the gain profile is practically uniform over nearly the whole active region, thus enhancing the excitation of the fundamental LP_{01} mode, it becomes extremely non-uniform at 380 K, when the gain in a broad central part of the active region is insignificant. Such profiles can favour higher-order transverse optical modes in larger active regions.

The wavelengths λ of the emitted radiation at the lasing thresholds as a function of the maximal active-region temperature increase $\Delta T_{A,max}$ over the ambient RT are plotted in figure 7. While the wavelength of the emitted radiation increases with temperature nearly linearly at the rate of 0.069 nm K^{-1}, the analogous change of the wavelength corresponding to the maximal gain is much faster (0.47 nm K^{-1}). Both numbers are very close to reported
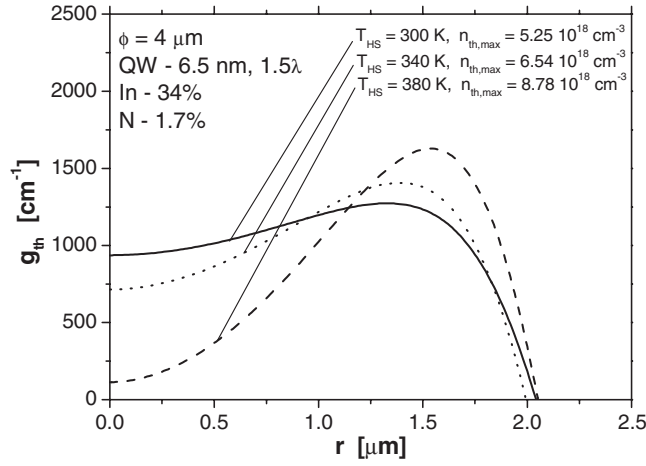
Figure 6. Radial profiles of the threshold optical gain at the temperatures indicated determined for the 1.5λ-cavity GaAs-based OC 6.5 nm $Ga_{0.66}In_{0.34}N_{0.017}As_{0.983}$/GaAs DQW VCSELs. Maximal values of the threshold active-region carrier concentrations, $n_{th,max}$, are shown.
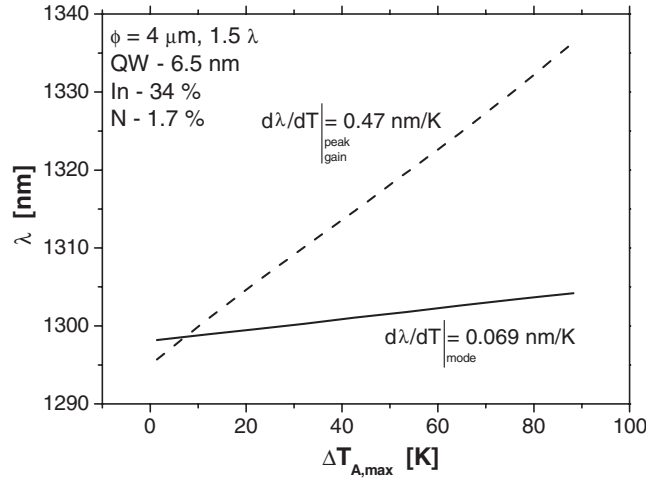

Figure 7. The emitted wavelength λ versus the maximal active-region temperature increase $\Delta T_{A,max}$ over the ambient RT shown for the 1.5λ-cavity GaAs-based OC 6.5 nm $Ga_{0.66}In_{0.34}N_{0.017}As_{0.983}$/GaAs DQW VCSELs. The wavelength changes corresponding to the maximal gain are also shown (dashed line).

experimental results of Reinhardt *et al* (2000) and Gollub *et al* (2002) as well as those of Kitatani *et al* (1997), Sato and Satoh (1999) and Yang *et al* (2000), respectively.

Figure 8 illustrates active-region temperature dependences of threshold currents I_{th} for various (GaIn)(NAs)/GaAs DQWs. Additionally, values determined for the characteristic temperature T_0 used to describe the above temperature changes:

$$I_{th}(T_A + \Delta T_A) = I_{th}(T_A) \exp\left(\frac{\Delta T_A}{T_0}\right) \tag{21}$$

are indicated, where T_A is the reference active-region temperature, and ΔT_A its increase. Basically, equation (21) and the parameter T_0 itself are often considered to be inappropriate for
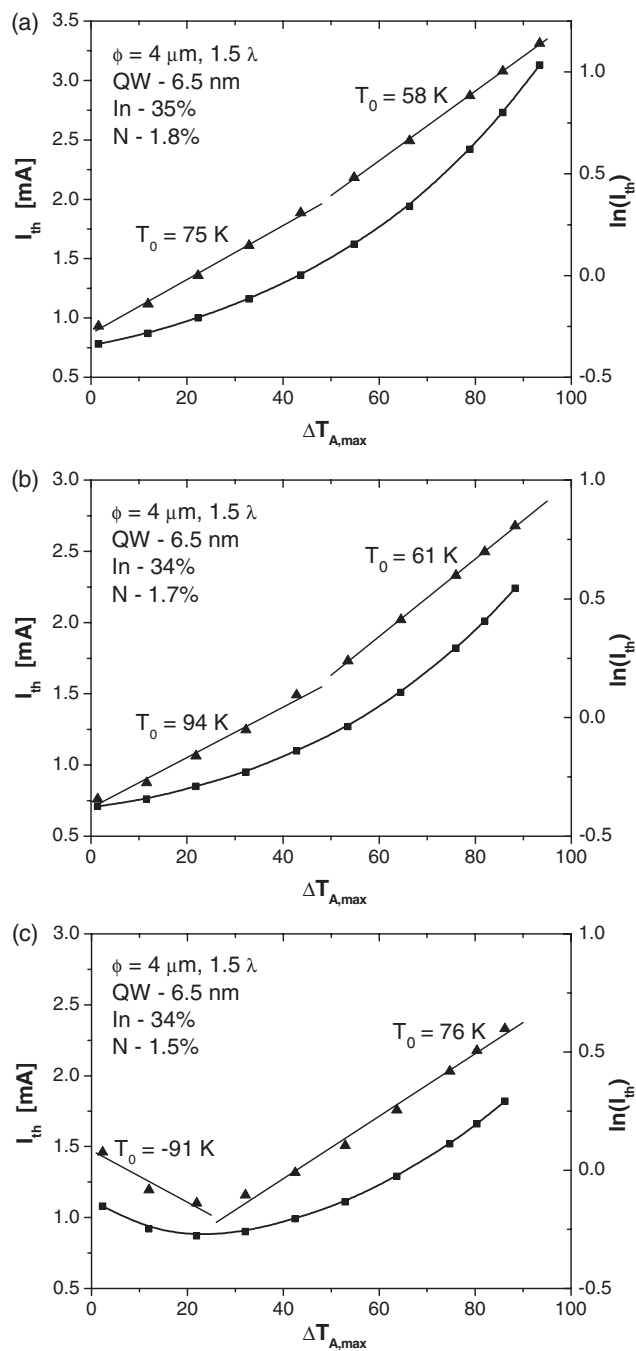
Figure 8. Threshold currents I_{th} for various (GaIn)(NAs)/GaAs DQWs: (a) $Ga_{0.65}In_{0.35}N_{0.018}As_{0.982}$/GaAs, (b) $Ga_{0.66}In_{0.34}N_{0.017}As_{0.983}$/GaAs and (c) $Ga_{0.66}In_{0.34}N_{0.015}As_{0.985}$/GaAs as a function of the maximal temperature increase $\Delta T_{A,max}$ over the RT. The values determined for the characteristic temperature T_0 are also shown.

VCSELs, because the temperature dependence of the VCSEL lasing threshold is associated not only with temperature changes of both the optical gain and the optical losses, as in edge-
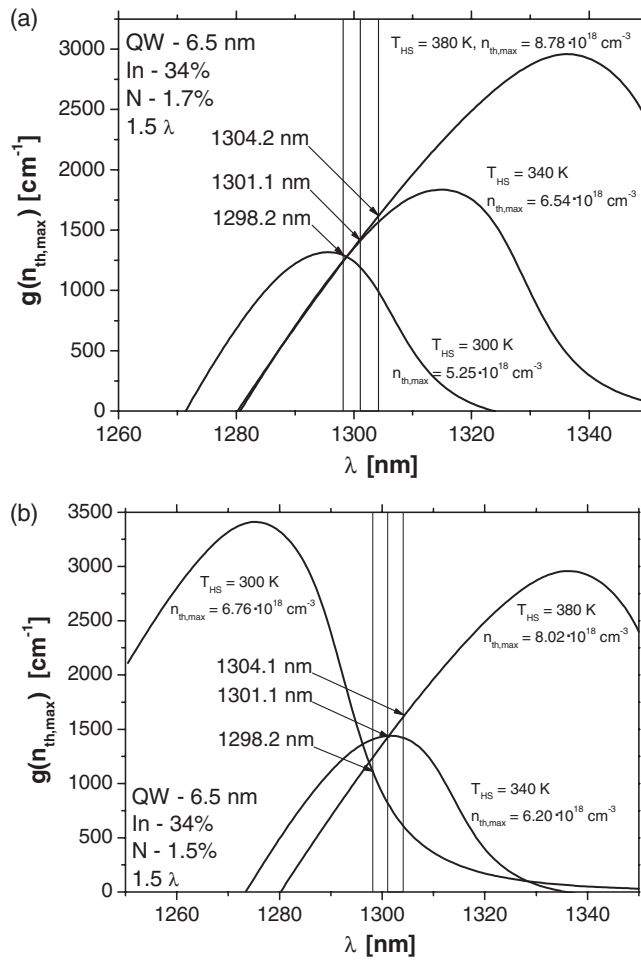
Figure 9. Gain spectra at lasing thresholds and various heat-sink temperatures T_{HS} for the indicated maximal values of the active-region carrier concentrations $n_{th,max}$ plotted for: (a) the $Ga_{0.66}In_{0.34}N_{0.017}As_{0.983}$/GaAs DQW and (b) the $Ga_{0.66}In_{0.34}N_{0.015}As_{0.985}$/GaAs DQW. Wavelengths of emitted radiation are also given.

emitting lasers, for which the above equations were originally proposed, but also with the spectral arrangement of the peak gain and the single longitudinal lasing mode. Nevertheless, the parameter T_0 may still be used for VCSELs, accepting, however, its possible negative values. As one can see in figure 8, the above-mentioned curves depend very strongly on even seemingly meaningless changes in the composition of the QW medium. It is also seen in figure 8(c) that threshold currents may even be reduced with increase in temperature as a result of better alignment of spectral positions of the mode and the peak gain. Then the parameter T_0 becomes negative. The effective value of the parameter T_0, determined for the temperature increase of 90 °C over RT, is found to increase from 65 K (figure 8(a)) to as high as 127 K (figure 8(c)).

The above strange behaviour is explained in figure 9, presenting gain spectra for the maximal value of the threshold carrier concentration and different heat-sink temperatures. Two active regions, considered in figures 8(b) and (c), are analysed in figures 9(a) and (b),
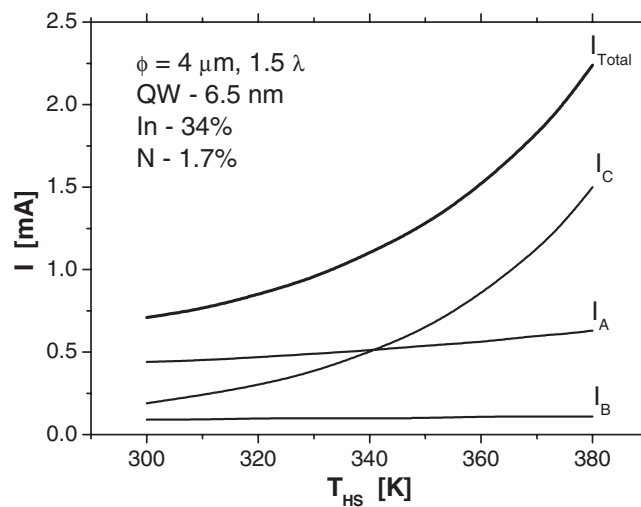
Figure 10. The total threshold current (I_{Total}) of the 1.5λ-cavity GaAs-based OC 6.5 nm $Ga_{0.66}In_{0.34}N_{0.017}As_{0.983}$/GaAs DQW VCSELs and its three parts associated with the monomolecular (I_A), the bimolecular (I_B) and the Auger (I_C) recombination as a function of the heat-sink temperature T_{HS}.

respectively. When at RT the emitted wavelength λ is placed close to the maximal gain value, as in figure 9(a), an increase in temperature over RT is followed by a rapid shift of λ along the high-energy part of the spectrum, because the gain spectrum is shifted more quickly (see figure 7). Therefore, to achieve enhancement to a suitable gain at λ, much higher carrier-concentration values are necessary at higher temperatures. To put this simply, the gain spectrum is fitted in this case with the emitted wavelength only at RT. Quite a different situation is shown in figure 9(b). This time, at RT, the emitted wavelength is intentionally shifted towards higher wavelengths; a higher RT lasing threshold follows. Then an increase in temperature over RT gives a better fitting of λ and the gain spectrum and, as a consequence, a lower lasing threshold in spite of the decreasing gain amplitude and increasing lasing losses. Thus a deliberate detuning of the lasing mode at RT from the active-region optical gain designed for the 1.3 μm emission ensures better device operation at higher temperatures and/or for higher device excitation.

Figure 10 shows the temperature dependences of three parts of the threshold current (cf equation (6)) associated with the non-radiative monomolecular recombination, the radiative bimolecular recombination and the Auger recombination, all in the 6.5 nm 1.5λ-cavity $Ga_{0.66}In_{0.34}N_{0.017}As_{0.983}$/GaAs DQW VCSEL. While at relatively low temperatures non-radiative recombination on point defects (I_A) composes the main part of the threshold current, the Auger recombination (I_C), as expected, becomes the most important recombination mechanism at higher temperatures. Surprisingly, radiative recombination (I_B) plays a secondary role in all the recombination phenomena in (GaIn)(NAs)/GaAs QWs.

The wavelength λ of the emitted radiation is shown in figure 11 (dashed curve) for the 6.5 nm 1.5λ-cavity $Ga_{0.65}In_{0.35}N_{0.018}As_{0.982}$/GaAs DQW VCSEL and various active-region radii r_A. The solid curve presents maximal values of the RT threshold optical gain. The lowest-threshold optical modes are indicated. As one can see, the most desired single-fundamental-mode operation is possible in small VCSELs—in this case, for active-region radii not exceeding 3 μm. As expected, an increase in the active-region size is followed by increasing order of the lowest-threshold transverse modes. The 4 μm diameter VCSEL exhibits the lowest RT CW lasing threshold. Its sharp increase for smaller active regions is a consequence of increasing
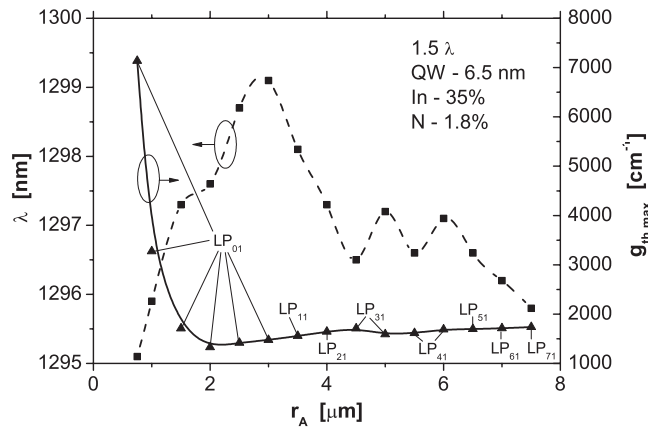
Figure 11. The wavelength λ of the emitted radiation (dashed curve) and the maximal threshold optical gain (solid curve) in the 6.5 nm 1.5λ-cavity $Ga_{0.65}In_{0.35}N_{0.018}As_{0.982}$/GaAs DQW VCSEL for various active-region diameters $\phi = 2r_A$. The lowest-threshold optical modes are indicated.
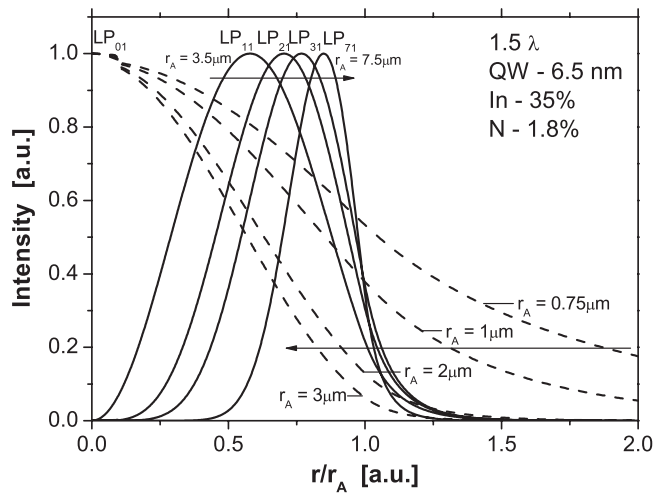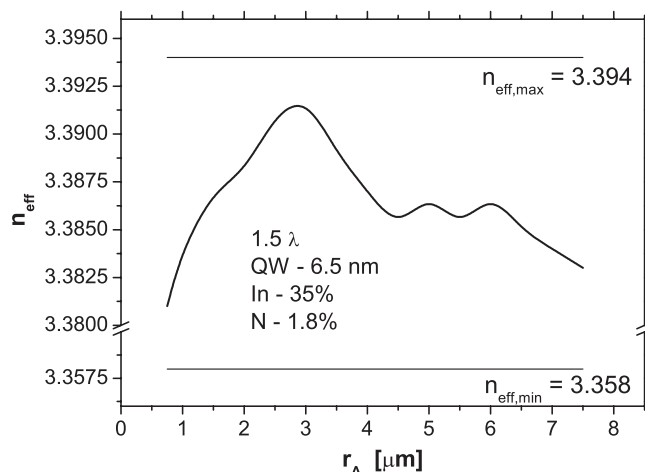

Figure 12. Radial profiles of the intensity of the lowest-threshold LP modes plotted for various radii r_A of the active region of the 6.5 nm 1.5λ-cavity $Ga_{0.65}In_{0.35}N_{0.018}As_{0.982}$/GaAs DQW VCSEL. Arrows indicate profile changes following an increase in the active-region radius.

penetration of passive areas surrounding the central active region (figure 12) by the radiation field of the LP_{01} mode which is followed by increasing diffraction and absorption losses. An increase in the active-region size, on the other hand, causes slight shifts of the radiation fields of the transverse modes of increasing order (figure 12), which are a result of the more non-uniform radial gain profiles.

The lasing wavelength of the emitted radiation (figure 11) is directly associated with the effective index of refraction, shown in figure 13. In particular, decreasing penetration of passive areas surrounding the central active region by the LP_{01} mode with increase in the active-region size from its minimal value is followed by steadily reducing influence of the low-refractive-index oxide layer (figure 13). Analogous oxide-induced changes of the effective index of refraction were reported for oxide-confined narrow-stripe (GaIn)(NAs)/GaAs diode lasers by Illek *et al* (2000).

Figure 13. The effective index of refraction of the lowest-threshold radiation mode versus the radii r_A of the active region of the 6.5 nm 1.5λ-cavity $Ga_{0.65}In_{0.35}N_{0.018}As_{0.982}$/GaAs DQW VCSEL. Both boundary index values, i.e. the lower one, determined for the hypothetical case of full oxidation of the AlAs layer, and the upper one, without this oxidation, are also shown.
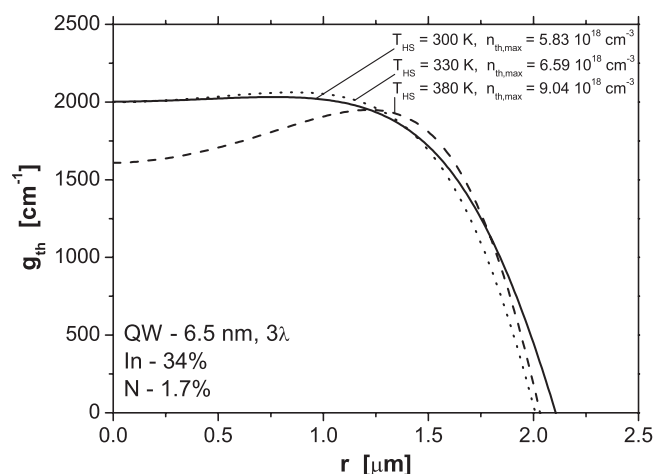
Figure 14. Radial profiles of the threshold optical gain at the temperatures indicated, determined for the 3λ-cavity GaAs-based OC 6.5 nm $Ga_{0.66}In_{0.34}N_{0.017}As_{0.983}$/GaAs DQW VCSELs. Maximal values of the threshold carrier concentration are shown.

4.3. The 3λ-cavity VCSELs

Let us consider now the 3λ-cavity VCSEL design. Figure 14 presents threshold gain radial profiles for within its active region of diameter $\phi = 2r_A = 4$ μm, analogous to the ones shown in figure 6 for the 1.5λ-cavity VCSEL. As one can see, at all heat-sink temperatures considered, slightly higher gain values (as compared to those for the 1.5λ-cavity VCSEL) are necessary to start the lasing, which corresponds to slightly higher values of the maximal threshold carrier concentrations. But, contrary to the behaviour of the 1.5λ-cavity VCSELs, the gain profiles of the 3λ-cavity VCSEL are only a little more non-uniform at higher temperatures than at RT,
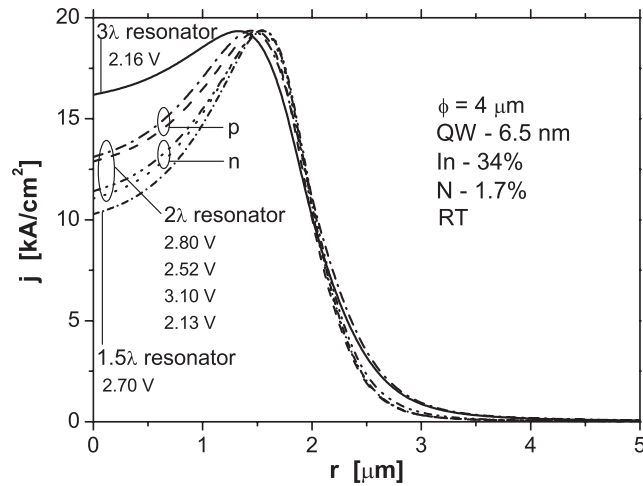
Figure 15. Radial profiles of the threshold current density at RT determined for the GaAs-based OC 6.5 nm $Ga_{0.66}In_{0.34}N_{0.017}As_{0.983}$/GaAs DQW VCSELs with different resonators: the 3λ cavity, 1.5λ cavity and four versions (described in the text) of the 2λ cavity. Threshold values for a device voltage are indicated.

which may be advantageous for device thermal properties, and which is directly associated with distinctly thicker current-spreading layers.

Let us consider the above effect in greater detail. For RT, radial threshold current density profiles are shown in figure 15 for the 3λ cavity, the 1.5λ cavity and four versions of the 2λ cavity. While in the 3λ cavity all three distances, between the upper DBR and the oxide aperture, between the oxide and the active region and between the active region and the bottom DBR, are equal to λ, they equal $\lambda/2$ in the 1.5λ cavity. In the case of the $2\lambda(p)$ cavity, as compared to the 1.5λ one, the upper curve corresponds to a double-thickness p-type layer over the oxide, whereas the bottom one corresponds to a double-thickness p-type layer below the oxide. Analogously, in the $2\lambda(n)$ cavity, the upper curve was plotted for the 280 μm thick lower-doping part of the n-type spacer (cf section 3) and the 82.5 μm higher-doping one, whereas the bottom curve was plotted for the opposite case. It is evident from figure 15, that improved high-temperature gain uniformity within the active region of the 3λ-cavity VCSEL (figure 14) follows from improved radial current spreading within the p-type spacer. Besides this, threshold values of the applied voltage are shown for all cases considered.

Gain spectra at lasing thresholds within the active region of the 3λ-cavity VCSEL design are plotted for different heat-sink temperatures in figure 16. They are analogous to the ones shown in figure 9(a) for the 1.5λ-cavity VCSEL. This time, however, the wavelengths of the emitted radiation are better fitted to moving gain spectra, which corresponds to a slower temperature increase in the threshold carrier concentration, especially at lower temperatures. As a result, the value of the parameter T_0 determined in figure 17 is then relatively high ($T_0 = 110$ K).

5. Conclusions

In the present paper, a comprehensive fully self-consistent optical–electrical–thermal–gain threshold model of oxide-confined quantum-well GaAs-based 1300 nm (GaIn)(NAs)/GaAs VCSELs is presented. The model enables a detailed analysis of the physics and operation
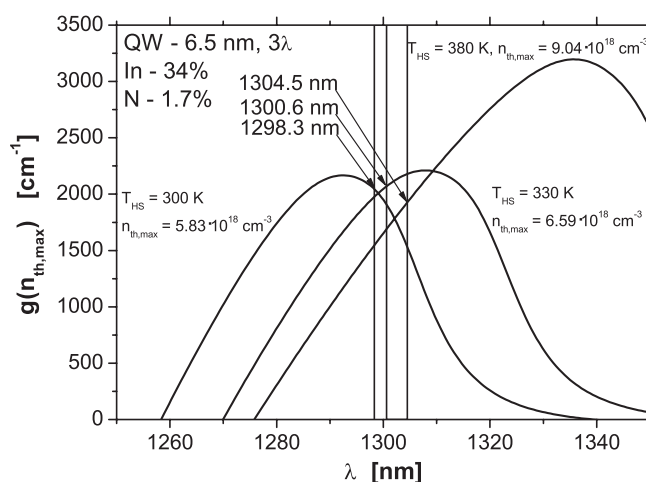
Figure 16. Gain spectra at lasing thresholds for various heat-sink temperatures T_{HS} plotted for the 3λ-cavity $Ga_{0.66}In_{0.34}N_{0.017}As_{0.983}$/GaAs DQW VCSEL. Maximal values of the threshold carrier concentrations and wavelengths of the emitted radiation are given.
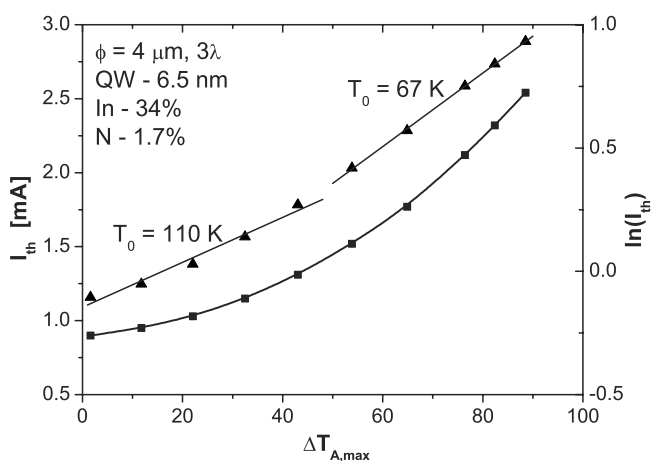
Figure 17. Temperature dependences of the threshold currents I_{th} for the 3λ-cavity $Ga_{0.66}In_{0.34}N_{0.017}As_{0.983}$/GaAs DQW VCSEL. The values determined for the characteristic temperature T_0 are also shown.

of the lasing devices considered, allowing a better understanding of their performance and a simulation of their anticipated operation characteristics. Besides this, the model may also be used to optimize their known structures as well as to design completely new structures corresponding to special features of the 1.3 μm OC (GaIn)(NAs)/GaAs QW GaAs-based diode lasers.

On the basis of our simulations, some guidelines for manufacturing low-threshold and high-mode-selectivity VCSEL devices are proposed. The 1.5λ-cavity VCSELs exhibit distinctly lower RT CW lasing thresholds than the 3λ-cavity ones. However, the latter VCSELs seem to offer better high-temperature performance. In particular, they enable single-fundamental-mode operation at higher ambient temperatures and they exhibit higher values of the parameter T_0. The latter effect may be also achieved in VCSELs with somewhat lower

nitrogen content in their active regions. As expected, single-fundamental-mode operation is possible in smaller VCSELs, e.g. for the 1.5λ-cavity ones, for active-region diameters not exceeding 6 μm. A deliberate detuning (towards higher wavelengths) of the lasing mode with respect to the active-region peak optical gain at RT ensures better device operation at higher temperatures and/or at higher device excitation.

Acknowledgments

References

Aboelfotoh M O, Borak M A and Narayan J 1999 *Appl. Phys. Lett.* **75** 3953–5

Adachi S 1994 *GaAs and Related Materials. Bulk Semiconducting and Superlattice Properties* (Singapore: World Scientific) pp 441–5

Anscombe N 2003 *Photon. Spectra* **37** 60–6

Babić D I, Piprek J and Bowers J E 1999 *Vertical Cavity Surface Emitting Lasers* ed C Wilmsen, H Temkin and L A Coldren (Cambridge: Cambridge University Press) chapter 9

Blakemore J S 1983 *J. Appl. Phys.* **53** R123–81

Carrére H, Arnoult A, Marie X, Amand T, Bedel-Pereira E, Potter R J and Balkan N 2003 *Physica* E **17** 245–6

Chuang S L 1995 *Physics of Optoelectronics Devices* (New York: Wiley)

Coldren C W, Larson M C, Spruytte S G and Harris J S 2000 *Electron. Lett.* **36** 951–2

Deria R J and Emanuel M A 1995 *Appl. Phys. Lett.* **77** 4667–72

Eliseev P G 1997 *Electron. Lett.* **33** 2046

Fehse R, Tomić S, Adams A R, Sweeney S J, O'Reilly E P, Andreev A and Riechert H 2002 *IEEE J. Sel. Top. Quantum Electron.* **8** 801–10

Gollub D, Fischer M, Kamp M and Forchel A 2002 *Appl. Phys. Lett.* **81** 4330–1

Grimmeiss H G and Monemar B 1971 *Phys. Status Solidi* a **5** 109–14

Harris J S Jr 2001 *IEEE LEOS Newsletter* **15** 16–8

Hetterich M, Dawson M D, Egorov A Yu, Bernklau D and Riechert H 2000 *Appl. Phys. Lett.* **76** 1030–2

Hetterich M, Grau A, Egorov A Yu and Riechert H 2003 *J. Appl. Phys.* **94** 1810–3

Illek S, Ultsch A, Borchert B, Egorov A Y and Riechert H 2000 *Electron. Lett.* **36** 725–6

Kitatani T, Kondow M, Nakatsuka S, Yazawa Y and Okai M 1997 *IEEE J. Sel. Top. Quantum Electron.* **3** 206–9

Kitatani T, Kondow M, Shinoda K, Yazawa Y and Okai M 1998 *Japan. J. Appl. Phys.* **37** 753–7

Kondow M, Uomi K, Niwa A, Kitatani T, Watahuki S and Yazawa Y 1996 *Japan. J. Appl. Phys.* **35** 1273–5

Larson M C, Coldren C W, Spruytte S G, Petersen H E and Harris J S 2000 *IEEE Photon. Technol. Lett.* **12** 1598–600

Lencefield D, Adams A R, Meney A T, Knap W, Litwin-Staszewska E, Skierbiszewski C and Robert J L 1995 *J. Phys. Chem. Solids* **56** 469–73

Nakwaski W 1988 *J. Appl. Phys.* **64** 159–66

Nakwaski W and Osiński M 1993 *IEEE J. Quantum Electron.* **29** 1981–95

Osiński M and Nakwaski W 2003 *Vertical-Cavity Surface-Emitting Laser Devices* (Berlin: Springer) chapter 5, pp 135–92

Pessa M, Pengg C S, Jouhti T, Pavelescu E-M, Li W, Karirinne S, Liu H and Okhotnikov O 2003 *Microelectron. Eng.* **69** 195–207

Ramakrishnan A, Steinle G, Supper D, Stolz W and Ebbinghaus G 2003 *J. Cryst. Growth* **248** 457–62

Reinhardt M, Fisher M, Kamp M, Hofmann J and Forchel A 2000 *IEEE Photon. Technol. Lett.* **12** 239–41

Riechert H, Ramakrishnan A and Stenle G 2002 *Semicond. Sci. Technol.* **17** 892–7

Sarzała R P and Nakwaski W 1997 *IEE Proc., Optoelectron.* **144** 421–5

Sato S, Osawa Y and Saitoh T 1997 *Japan. J. Appl. Phys.* **36** 2671–5

Sato S and Satoh S 1999 *Electron. Lett.* **35** 1251–2

Seo W-H and Donegan J F 2003 *Appl. Phys. Lett.* **82** 505–7

Sfigakis F, Paddon P, Pacradouni V, Adamczyk M, Nicoll C, Cowan A R, Tiedje T and Young J F 2000 *J. Lightwave Technol.* **18** 199–202

Shan W, Walukiewicz W, Yu K M, Ager J W III, Haller E E, Geisz J F, Friedman D J, Olson J M, Kurtz S R, Xin H P and Tu C W 2001 *Phys. Status Solidi* b **223** 75–85

Shirakata S, Kondow M and Kitatani T 2001 *Appl. Phys. Lett.* **79** 54–6

Skierbiszewski C 2002 *Semicond. Sci. Technol.* **17** 803–14

Spitzer W G and Whelan J M 1959 *Phys. Rev.* **114** 59–63

Steinle G, Mederer F, Kircherer M, Michalzik R, Kristen G, Egorov A Y, Riechert H, Wolf H D and Ebeling K J 2001a *Electron. Lett.* **37** 632–4

Steinle G, Riechert H and Egorov A Yu 2001b *Electron. Lett.* **37** 93–5

Tanguy C 1996 *J. Appl. Phys.* **80** 4626–31

Tansu N and Mawst L J 2003 *Appl. Phys. Lett.* **82** 1500–2

Thurmond C D 1975 *J. Electrochem. Soc.* **122** 1133–41

Tomic S and O'Reilly E P 2002 *Physica* E **13** 1102–5

Ueng U J, Chen N-P, Janes D B, Webb K J, McInturff D T and Melloch M R 2001 *J. Appl. Phys.* **90** 5637–41

Wenzel H and Wünsche H-J 1997 *IEEE J. Quantum Electron.* **33** 1156–62

Yang K, Hains C P and Cheng J 2000 *IEEE Photon. Technol. Lett.* **12** 7–9